

Chalcogen Impurity Barriers in 2D Systems via Semi-Empirical/Machine Learning Modeling: A Survey over 4000 Materials

M. L. Pereira, Jr,^{†,‡} M. G. E. da Luz,[¶] P. Cesana,[§] A. L. da Rosa,^{||} M. J. Piotrowski,[⊥] D. Guedes-Sobrinho,[#] T. A. S. Pereira,^{@,Δ,∇} E. A. Moujaes,^{††} A. C. Dias,^{‡‡} and R. M. Tromer^{*,¶¶}

[†]*University of Brasília, College of Technology, Department of Electrical Engineering, Brasília-DF, 70910-900, Brazil.*

[‡]*Rice University, Department of Materials Science and NanoEngineering, Houston-TX, 77005, United States*

[¶]*Departamento de Física & Multidisciplinary Laboratory for Modeling and Analysis of Data in Complex Systems (MADComplex), Núcleo de Modelagem e Computação Científica-Centro Interdisciplinar de Ciência, Tecnologia e Inovação, Universidade Federal do Paraná, 81531-980 Curitiba-PR, Brazil*

[§]*Institute of Mathematics for Industry, Kyushu University, 744 Motooka, Fukuoka 819-0395, Japan*

^{||}*Institute of Physics, Federal University of Goiás, Campus Samambaia, 74690-900, Goiânia, Goiás, Brazil.*

[⊥]*Department of Physics, Federal University of Pelotas, PO Box 354, Pelotas, RS, 96010 – 900, Brazil*

[#]*Chemistry Department, Federal University of Paraná, CEP 81531 – 980, Curitiba, Brazil*

[@]*Physics Graduate Program, Institute of Physics, Federal University of Mato Grosso, Cuiabá, MT, Brazil*

^Δ*Instituto de Física, Universidade Federal Fluminense, 24210-346, Niterói, Rj, Brasil*

[∇]*National Institute of Science and Technology on Materials Informatics, Campinas, Brazil*

^{††}*Institute of Physics, Federal University of Bahia, Campus Ondina, 40170-115, Salvador, BA, Brazil.*

^{‡‡}*Institute of Physics and International Center of Physics, University of Brasília, 70919-970, Brasília, DF, Brazil.*

^{¶¶}*University of Brasília, Institute of Physics, Brasília-DF, 70910-900, Brazil*

E-mail: raphael.tromer@unb.br

Abstract

Adequate characterization of two-dimensional (2D) materials with low energy barriers for impurity adsorption is key for advancing applications based on catalysis, sensing, and surface functionalization. However, first-principles methods, such as Density Functional Theory

(DFT), are often computationally extremely expensive for feasible large-scale screenings. Given such a scenario, we address a data-driven approach which integrates the semi-empirical Extended Hückel Method (EHM) with machine learning (ML) techniques to estimate adsorption energy barriers in the case of three relevant chalcogen impurities, sulfur (S), selenium (Se)

and tellurium (Te). With this aim, we consider the 4036 2D materials found in the Computational 2D Materials Database (C2DB). The scheme employs the EHM to compute energy profiles along three in-plane migration paths, from which average barriers can be derived. The equilibrium distance between the impurity and the 2D surface is not calculated from a time-consuming geometry optimization. Instead, it is estimated from a simple effective phenomenological expression. Physicochemical descriptors are then obtained from the Matminer (Materials Data Mining) library for curated features. Four different ML models are tested, with the XGBoost (considering hyperparameter optimization via Optuna) leading to the highest performance. We further use SHAP to verify the resulting predictions, focusing on the $\sim 1,500$ materials displaying the lowest barrier values. As it could be anticipated, we establish that the average valence electron count, electronegativity, and atomic number are typically the most relevant attributes to validate the ML model. But we also are able to determine, for the different chalcogen atoms, which other few descriptors likewise considerably influence the adsorption properties. Our results show that when combined with interpretable ML protocols, EHM (and potentially semi-empirical calculations in general) can produce a scalable framework for choosing 2D structures that exhibit the desired capture/release dynamics pertinent in a variety of utilization.

Introduction

Two-dimensional (2D) materials have emerged as one of the most promising classes of systems for advanced technological applications, owing to their unique physical and chemical properties. In special, transition metal dichalcogenides (TMDs) — examples being, molybdenum disulfide (MoS_2), diselenide (MoSe_2) and ditelluride (MoTe_2) — exhibit outstanding electronic, optical, mechanical, and catalytic characteristics.¹⁻⁴ Such versatility positions TMDs as attractive candidates for various usages, including flexible electronics, high-performance

sensors, optoelectronic devices, photocatalysis, and emerging energy storage technologies.

Among the distinct properties of these 2D layered systems, the energy barrier arising from the interaction with atoms or molecules is particularly crucial. Indeed, this plays a central role in several physicochemical processes, such as molecular adsorption,⁵ charge transfer,⁶ surface catalysis,⁷ and chemical sensing.⁸ Hence, when focusing on particular utilization, assessment of appropriate structures with low energy barrier values across a wide range of TMDs may be essential.⁹

Density Functional Theory (DFT) stands out as one of the primary calculation tools for accurately obtaining nanomaterials' structural and electronic properties. However, DFT's high computational cost significantly limits its systematic application to the evaluation of energy barriers over big material datasets.^{10,11} This limitation poses a significant obstacle to a large-scale exploration of promising systems, such as those in the Computational 2D Materials Database (C2DB). Actually, the C2DB comprises thousands of 2D compounds, most of them still largely unexplored.¹²

Given such a scenario, a possible alternative is then to employ semi-empirical methods. In this direction, the Extended Hückel Method (EHM) provides a low-cost computational approach for large-scale energy estimations.^{13,14} Although less accurate than DFT (due to the lack of full geometry optimizations and the absence of explicit band structure inputs), the EHM is highly useful in screening total energies of big pools of nanostructures,¹⁵ eventually as a first selective procedure for the best candidates in practical times. For example, such a strategy has already been shown to work well in predicting the adsorption energy of contaminants on 2D surfaces,¹⁶⁻²⁰ including the case of alkali metals (Na, K, and Li) with graphene.²¹⁻²³

In parallel, machine learning (ML) techniques have revolutionized the study of material features, enabling the efficient prediction of complex physical quantities from a limited number of reference calculations.²⁴ Moreover, the application of ML in high-throughput probing should facilitate trend identification and accel-

erate the uncovering of materials with tailored properties. Certainly, a critical step in the scheme is the construction of representative descriptors for the systems under scrutiny. But a robust tool to address such difficulty is the *Matminer* (Materials Data Mining) library, skillfully generating effective quantitative representations for ML models.²⁵

Among the many available supervised learning algorithms, XGBoost (Extreme Gradient Boosting) has emerged as a high-performance protocol for handling heterogeneous elaborated datasets.^{26,27} Further, to enhance model interpretability, techniques such as SHAP (SHapley Additive exPlanations) have been increasingly considered, allowing for the quantification of descriptors importance and for the inference of actual physical correlations. This establishes explicit connections between the most relevant features and the underlying physicochemical mechanisms governing the system predicted properties.^{28,29}

Here we develop a novel framework to investigate energy barriers in 2D structures by integrating EHM with advanced ML techniques. We then address chalcogen atoms, specifically, Sulfur (S), Selenium (Se), and Tellurium (Te), interacting with 2D materials surfaces. We take into account the problem geometry through a phenomenological, nevertheless rather simple and effective, expression based on the covalent radii of the adsorbates. It gives the fixed equilibrium distance between the atom and the 2D surface. From the proposed methodology, we estimate the energy barriers for over 4,000 systems retrieved from the C2DB database. The obtained large dataset is thus used to train predictive models (in different ranges of energy) employing the XGBoost — for sake of comparison, other ML procedures are also tested. Finally, analyzes considering the SHAP protocol for the 1,495 materials with the lowest barriers lead to accurate predictions and tangible physical interpretation of the factors governing energy barriers in these structures. The generality of the whole procedure might constitute a relevant new approach for studying distinct aspects of atoms deposition on 2D materials.

Methodology

In the present study we follow a sequential protocol that involves (see the workflow in Fig. 1): (i) to built an energy barrier dataset (steps 01 and 02); (ii) to extract physicochemical descriptors for numerical representation of each two-dimensional system (step 03); and (iii) to implement ML models based on the physicochemical descriptors (step 04) and then to physically interpret the obtained results (step 05).

For the actual systems, we accessed one of the most comprehensive repository of 2D structures, the C2DB,¹² covering a rich diversity of configurations, symmetries, and fundamental physicochemical properties. It comprises an extensive collection of 2D materials, from experimentally synthesized ones, such as graphene, to compounds proposed either theoretically or identified through AI-assisted simulations.

Our framework steps are described below.

Semi-empirical calculations

For each structure available in the C2DB, we estimated the energy barrier associated with the adsorption of three types of dichalcogenide impurities, sulfur (S), selenium (Se), and tellurium (Te), by employing the EHM, as in the YAeHMOP software package.³⁰ This semi-empirical method can calculate the system total energy, but without performing any geometry optimization, which requires a predefined equilibrium distance d_{eq} between the impurity and the 2D surface; refer to Fig. 2. This d_{eq} is thus estimated from the scheme proposed in Sec. .

Each 2D material was expanded into a $2 \times 2 \times 1$ supercell, and a reference atom was selected as the one closest to the origin within the xy plane. The impurity was initially placed above this reference atom at the equilibrium distance d_{eq} . Subsequently, the impurity was displaced along three distinct in-plane trajectories: the x axis, the y axis, and the xy diagonal. Each trajectory spanned a displacement of approximately 3 Å, beyond which edge effects — due to the cluster approximation adopted in YAeHMOP for periodic boundary conditions — began to introduce non-physical artifacts in the energy

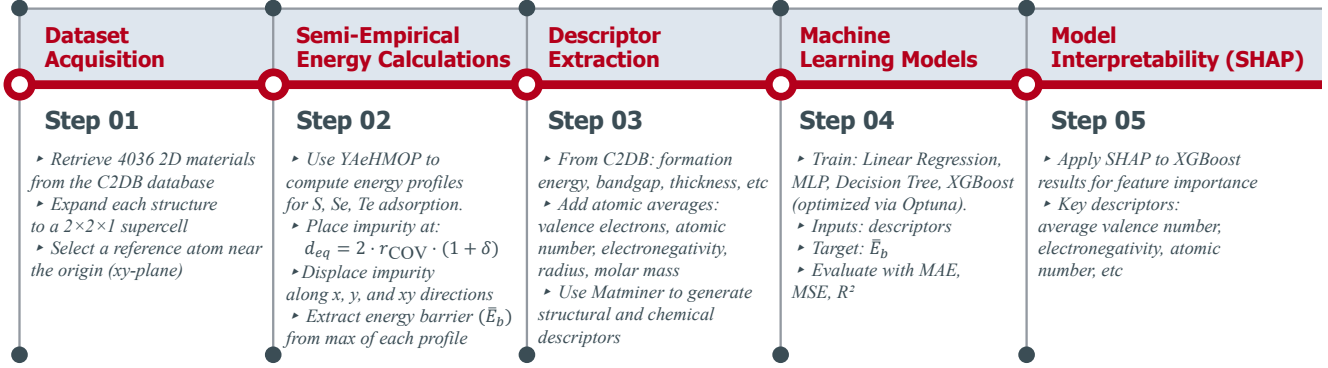


Figure 1: Workflow summarizing all the data gathering, calculations, ML models and interpretative analyzes implemented to properly characterize the adsorption of chalcogen atoms in 2D materials classified in the C2DB database (comprising 4000+ distinct systems).

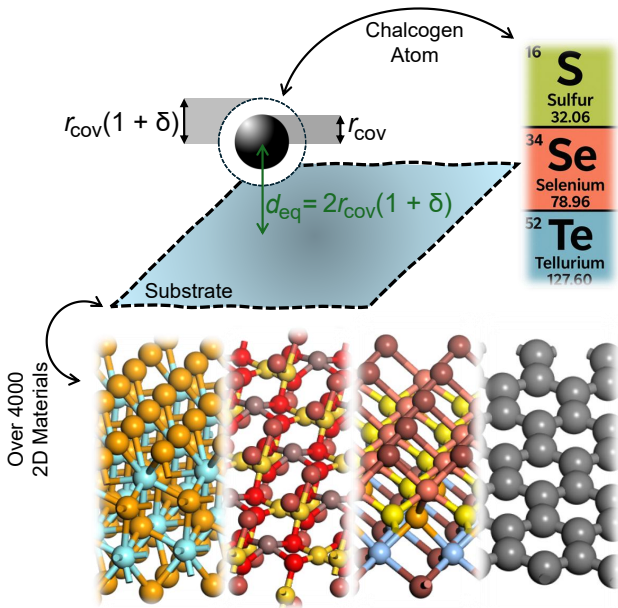


Figure 2: Schematics of the problem geometry. Distinct 2D material (from the C2DB database) constituting the substrate for a chalcogen atom (either S, Se or Te) adsorption. The effective equilibrium distance d_{eq} , used to calculate the energy barriers, is estimated from the phenomenological considerations in Sec. .

profile. Therefore, three energy barrier curves were generated for each system, corresponding to the three directions. The average energy barrier was computed as

$$\bar{E}_b = \frac{1}{3} (E_b^x + E_b^y + E_b^{xy}), \quad (1)$$

where the maximum value from each energy

profile was selected as the target variable for ML models.

The semi-empirical equilibrium distance

Two-dimensional materials are often characterized by in-plane covalent bonds and out-of-plane van der Waals interactions.³¹ The latter being responsible, for example, for the separation distance between graphene sheets in distinct bilayer structures (typically in the range $3.25 \sim 3.50 \text{ \AA}$)³² and for atom adsorption.^{33,34} Thus, the van der Waals radius³⁵ — associated to an effective size for the interfacial adhesion mechanism — is one of the main factors determining the equilibrium distance h_{eq} between the adsorbed atom and distinct points along the 2D material surface.³⁶ Moreover, some findings in the literature^{37,38} have pointed out that atom adsorption in 2D materials tend to display rather simple universal relations to the adsorbent structure geometrical symmetries. Hence, in a first order approximation, where we suppose an effective equilibrium distance d_{eq} for the full surface, such a configuration parameter can be assumed fairly independent on specific details of the atoms and 2D materials involved (but see additional discussion in section).

Based on the aforementioned, we propose to set $d_{eq} = 2r_{vdW}$, with r_{vdW} the van der Waals radius. Nonetheless, it has been long known^{35,39} that for a large number of situations $r_{vdW} - r_{cov} = \Delta_r > 0$, for r_{cov} the atom covalent radius and Δ_r reasonably constant. So, d_{eq} can

be written as (see the schematics in Fig. 2)

$$d_{\text{eq}} = 2 r_{\text{cov}} (1 + \delta), \quad (2)$$

where $\delta = \Delta_r / r_{\text{cov}}$.

For weak van der Waals bonding (like in gases, liquids and polymers), the Pauling rule proposes that $\Delta_r|_{\text{Pauling}} = 0.8 \text{ \AA}$, a value put in solid grounds in ref.³⁹ For the clearly tighter attraction between adsorbed atoms and 2D materials,^{33,34} such Δ_r must be smaller. So, based on some estimations in the literature (see, e.g., scheme 5 and Sec. 5.4 of ref.⁴⁰) we assume $\Delta_r \sim \Delta_r|_{\text{Pauling}}/2 = 0.4 \text{ \AA}$. Given that the three atoms of interest here are S, Se and Te of r_{cov} , respectively, equal to 1.02 \AA , 1.2 \AA and 1.36 \AA , we get $\delta \approx 0.3$. So, Eq. (2) with $\delta = 0.3$ is the expression we consider throughout this work.

We remark that as a further support for the approximation in Eq. (2), it properly reproduces average h_{eq} 's from DFT calculations for alkali metal atoms (Na, K, Li) interacting with graphene and other 2D surfaces.^{21–23}

The physicochemical descriptors

To numerically characterize each system (see Fig. 1, step 03), we considered a set of physicochemical descriptors derived directly from the C2DB database; as examples we cite formation energy, monolayer thickness, and electronic band gap. These were complemented by externally computed attributes, including average: valence electrons, atomic number, atomic radius, electronegativity and molar mass. In addition, we employed the Matminer library,²⁵ which provides a broad range of automated descriptors based on chemical composition, crystal structure, and electronic features. Matminer has been widely adopted in materials informatics due to its ability to generate robust, interpretable, and reproducible properties for usage in ML pipelines.⁴¹

The totality of these features, namely, those directly from the C2DB, plus the computed attributes, plus those from the Matminer, we call the Full Set of Descriptors, FSD.

The ML and interpretability models considered

The generated and assembled dataset of descriptors, the FSD, was considered to evaluate and compare the performance of four supervised learning algorithms. The first was a simple model that assumes a linear relationship between the descriptors and the target energy barrier. Although interpretable and straightforward, linear regression is naturally insufficient for systems with considerable nonlinear trends.⁴² Next, we employed a multilayer perceptron (MLP) neural network, capable of capturing complex polynomial patterns, nonetheless requiring great amount of data and hyperparameter tuning.⁴³ As a third possibility, we tested a decision tree model, which works through hierarchical decision rules by partitioning the descriptor space. While highly interpretable, this approach is susceptible to overfitting noisy data.⁴⁴

Lastly, we assumed the XGBoost algorithm, a powerful ensemble method based on gradient-optimized decision trees. XGBoost is greatly recognized for its highly predictive accuracy, resilience to overfitting, and excellent performance across large and heterogeneous datasets. Indeed, in our analyzes this scheme outperformed all the other three protocols.²⁶

To interpret the outputs of the ML models and to identify the most influential features governing energy barrier predictions, we used the SHAP method.²⁸ Based on cooperative game theory, SHAP assigns a Shapley value to each input feature, quantifying its marginal contribution to the model's prediction. SHAP has lately earned considerable popularity in materials science. It allows to give concrete interpretations to results obtained from complex black-box models. In other words, SHAP helps to link physical attributes to forecast behavior from AI-based methodologies. This is fundamental to ascribe phenomenological significance to context-free procedures, especially if one is trying to unveil the physical-chemical mechanisms underlying the properties of a material.⁴⁵

Results

A relevant benchmark: graphene as substrate

We start our analysis supposing graphene as the 2D substrate for the S, Se and Te dichalcogenide elements, given the graphene well-known physical and chemical properties and its widespread usage as a reference in surface science. So, this is an ideal case (a benchmark) to validate the consistency and reliability of the proposed semi-empirical methodology.

We present the energy barrier profiles obtained for S, Se and Te, respectively, in Fig. 3(a), 3(b) and 3(c). Each graph displays the variation in the energy barrier as function of a generalized reaction coordinate, corresponding to three distinct in-plane diffusion paths for the impurity along the: x (blue), y (orange), the diagonal xy (green), directions. These trajectories simulate the lateral migration of the adsorbate along the 2D surface, allowing to characterize directional effects on diffusion. We recall that as discussed in Sec. , the displacements were limited to approximately 3 \AA , a constraint introduced to reduce edge effects from the simplified periodic boundary condition treated via cluster approximation by YAeHMOP software.

As clear from Fig. 3(a), the energy barrier profile for S shows marked anisotropy among the x and y displacement directions. Indeed, the highest barrier takes place along the y direction, peaking at approximately 1.02 eV , whereas the lowest barrier lies along the x direction, reaching only 0.66 eV — but for a profile which is almost constant. Mostly influenced by y (in fact, closely following it), the xy path has a peak at 0.98 eV . This pronounced directional dependence seems to be attributed to the graphene surface’s local electronic topology and the S atom’s preferential adsorption orientation. Notably, anisotropic interactions have been reported in DFT-based computations,^{46,47} arising from variations in the registry between the impurity and the graphene lattice. Energy barrier values for S on various surfaces typically range from 0.5 to 1.2 eV , depending on the adsorption site and surface coverage.⁴⁸ Our much

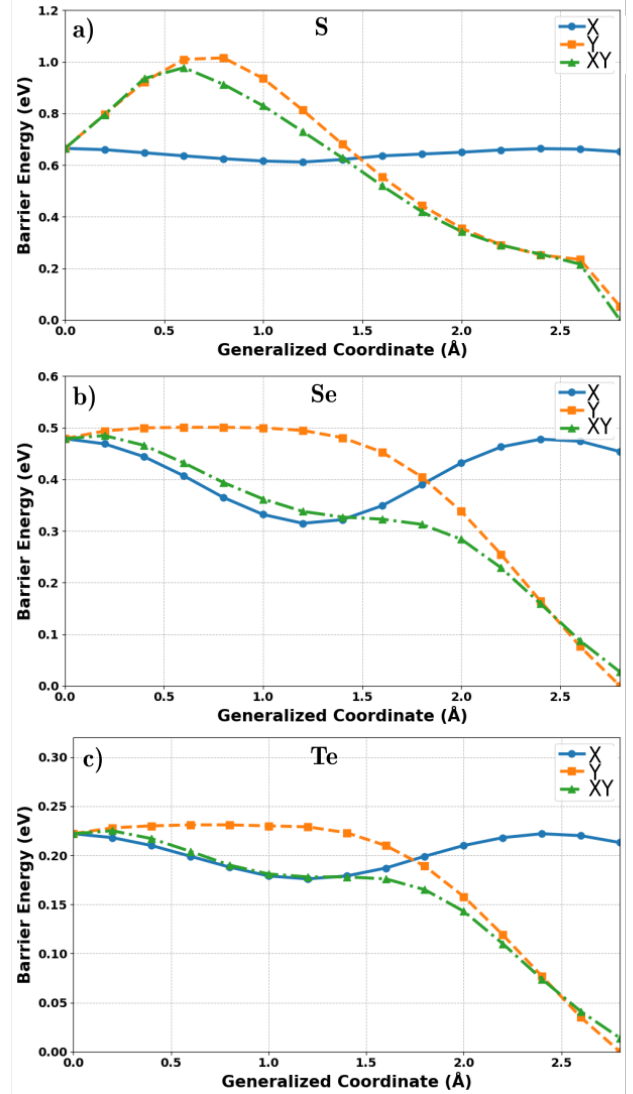


Figure 3: Energy barrier profiles (in eV) obtained for the dichalcogenide elements: (a) S, (b) Se, and (c) Te, adsorbed on graphene using the EHM via the YAeHMOP software. In each case, the impurity was displaced along three directions over the graphene surface: x (blue), y (orange), and the diagonal xy (green).

simpler semi-empirical calculations fall within this expected range.

Results for Se are depicted in Fig. 3(b). Note that overall it displays a shorter range of energy variation than S. The y direction continues to have the largest barrier, reaching a maximum of roughly 0.50 eV ; the x and xy directions show maximums that are only somewhat lower than it. Also, differently from S, for Se the xy path is now a more balanced combination of the be-

haviors along x and y . This decrease in magnitude and anisotropy might be attributed to the larger atomic radius and lower electronegativity of Se relative to S, weakening the orbital overlap with the graphene surface. Thus, the potential energy landscape becomes less corrugated, with shallower energy minima and maxima.

These trends are consistent with theoretical studies of Se adsorption in graphene and related 2D materials, where typical barriers of ~ 0.6 eV are often obtained.⁴⁷ This enhanced surface mobility of Se can have practical implications for surface functionalization, epitaxial growth, and thermally activated diffusion. Hence, further characterization through ML approaches may provide valuable insights into design and selection of functional materials (see later).

The barrier energies for Te are displayed in Fig. 3(c), exhibiting the lowest values among the three elements, although with general traits resembling Se. The maximum is approximately 0.23 eV for y and about 0.22 eV for the x and xy directions. The Te quasi-isotropic behavior (in terms of maximum barriers heights) reflects its larger polarizability and atomic radius, which lead to weaker and more delocalized interactions with the graphene surface. Consequently, the energy landscape becomes flatter and less sensitive to the diffusion direction. All this aligns with previous investigations of Te adsorption on graphene, yielding barriers usually below 0.3 eV.⁴⁹ Thus, the EHM properly captures the correct interaction energies relative magnitudes and key symmetry trends; critical features for the understanding of surface diffusion and transport phenomena.

An important qualitative point to be emphasized is that, despite the simplicity of the semi-empirical scheme used, particularly its lack of geometry optimization and electronic structure resolution, the order of the calculated energy barriers ($S > Se > Te$) concurs with the expected chemical tendency across the periodic table group 16: the increase in atomic radius and the decrease in electronegativity as one moves down the chalcogen group. This results in progressively weaker effective interactions between the impurity and the substrate.

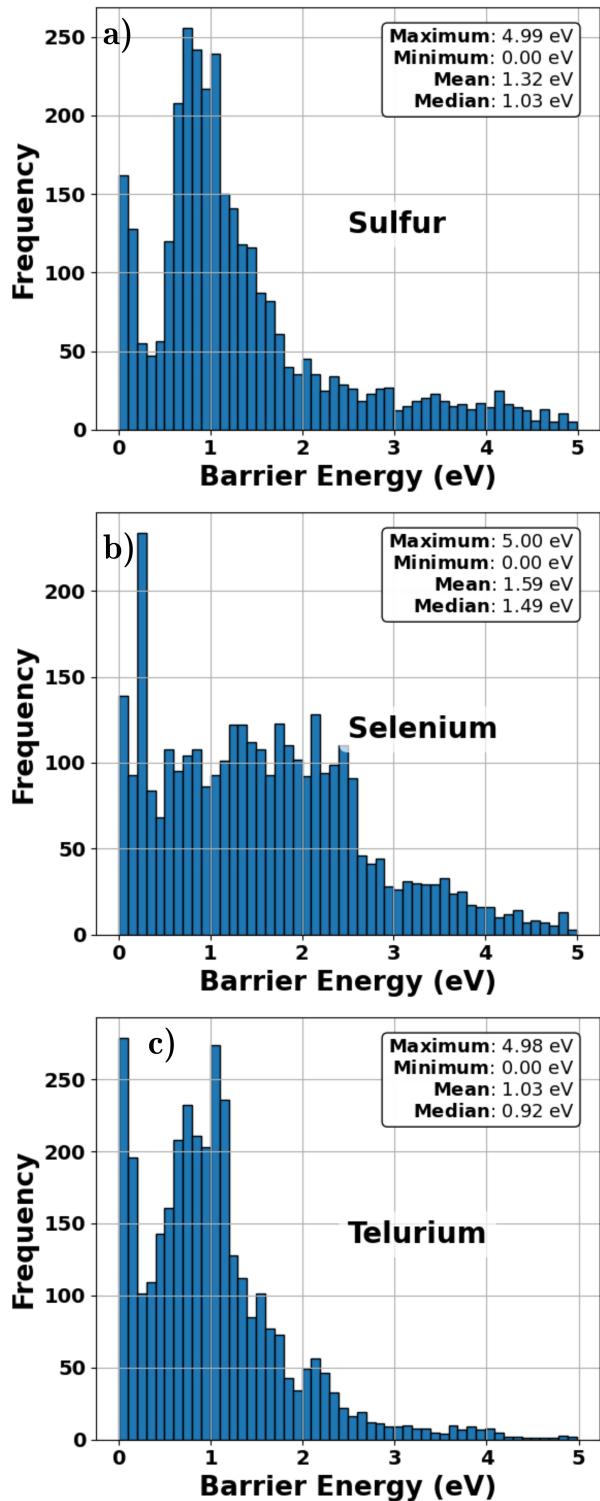


Figure 4: Histograms of average energy barriers for about 3150 2D systems from the C2DB database, for which the energies do not exceed 5.0 eV. The impurities are (a) S, (b) Se and (c) Te. The values represent the average over the three directions x , y , and xy .

Energy barrier computations for the full C2DB database

7 Having illustrated the reliability of the present approach for the paradigmatic graphene case,

next we apply our semi-empirical method to a rather large collection of systems. Indeed, for the 4036 2D materials from the C2DB database, each surface is doped with one of three dichalcogenide impurities. Then, the average energy barrier is calculated from the maximum energy barrier along the x , y , and xy directions; refer to Eq. (1). In Fig. 4 we summarize the simulations by means of histogram distributions (i.e., frequency or number of cases within a given energy interval, the bin). To simplify the analysis, we show only the materials with barrier energies up to 5.0 eV. This reduces the number of materials to about 3150 (78% of the original set) for each impurity atom, namely, S (Fig. 4(a)), Se (Fig. 4(b)), and Te (Fig. 4(c)).

We should emphasize that the C2DB comprises both already synthesized as well as theoretically predicted 2D systems. Moreover, it covers many distinct structural families. In this way, the present survey characterizes the energy barriers behavior across a great variety of 2D materials. On one hand, it pinpoints the variations in substrate interactions, influenced by structure, symmetry, and electronic properties. On the other hand, it unveils the differences in the chemical nature of the dichalcogenides adsorbing. Therefore, the histogram reveals certain coincidences as well as important distinctions between the three atoms.

As for similarities, for the energy interval considered, 0~5 eV, the majority of the examples are below 2.0 eV. Also, there is a considerable number of materials for which the barriers are in the range 0~0.3 eV. The mean and median for S, Se and Te are, respectively, 1.32 and 1.03 eV, 1.59 and 1.49 eV and 1.03 and 0.92 eV. So, the difference between the highest (Se) and lowest (Te) mean, of about 35%, is not so large.

Regarding the contrasts among S, Se and Te, we first observe that the histogram for S, Fig. 4(a), demonstrates a certain similarity among materials, with the principal mode being around 0.6~1.6 eV. Then, there is a long tail extending toward higher energies (up to 5 eV). Consequently, the distribution exhibits a considerable skewness. Further, it shows that although most systems present moderate barriers, a significant number of surfaces have a

strong interaction with S. This is likely due to the Sulfur high propensity to form covalent bonds with the 2D materials orbitals of high electronic density. Such type of orbitals are particularly common in transition-metal-based structures.

In distinction, the Se histogram in Fig. 4(b) displays a broad plateau, with fairly similar frequencies in the energy range 0.6~2.5 eV. The average for Se is 1.59 eV, while for S it is 1.32 eV. Such a higher value can be attributed to a mildly lower electronegativity of Se, resulting in a more diffuse interaction with the surfaces, but which is still enough to yield relevant barrier values. Likewise, the tendency of a stronger orbital polarization for Se, that depends on the lattices symmetries — i.e., hexagonal, orthorhombic, etc — may also contribute to a wider range for the energy barrier values.

Overall, the histograms for S and Te, respectively, Fig. 4(a) and Fig. 4(c), display certain parallels, however differences are also identified. For instance, the distribution for Te exhibits a faster decreasing tale. Moreover, the number of surfaces having barrier energies in the range 0~0.3 eV for S is only of around 60% of those for Te. These facts lead to a mean of 1.03 eV for Te (the lowest among the three impurities), suggesting that generally Te interacts weakly with the 2D systems, the same trend found for graphene as a surface in the previous section. This should be expected, considering the Te larger atomic radius, lower electronegativity, and higher polarizability, when compared to S and Se. It is worth remarking that from DFT-based computations, nonetheless implemented for much fewer situations,⁴⁹ it has been demonstrated the somehow feeble binding nature of Te. Here, from our relatively inexpensive protocol, we have been able to extend such predictions for a rather big set of 2D materials.

ML models predictions for the barrier energies

In critical applications, such as those related to catalysis and building functionalized surfaces with adjustable diffusion characteristics, adsorbed atoms should exhibit high surface mo-

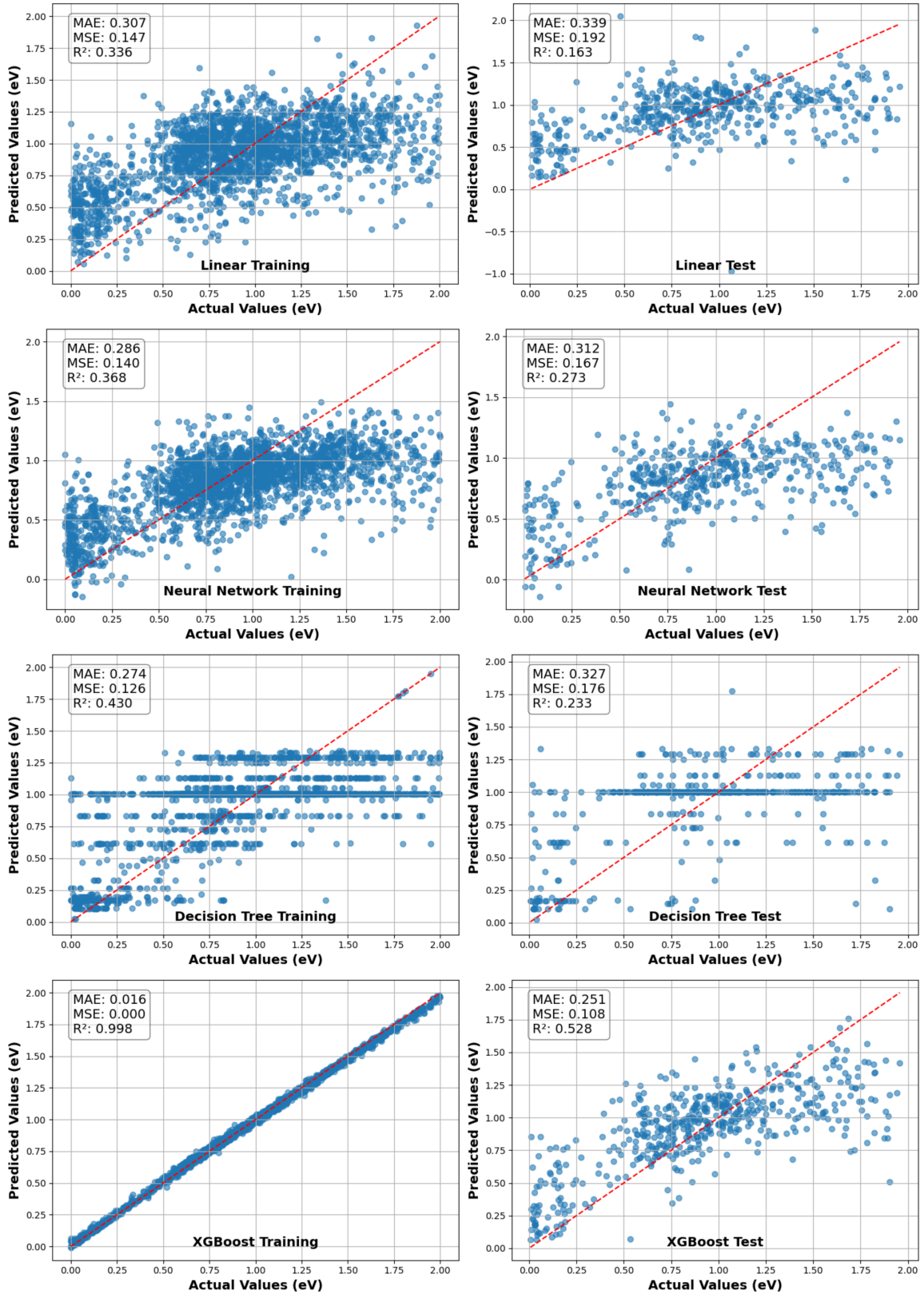


Figure 5: Comparison between the calculated and ML-predicted energy barrier values (≤ 2.0 eV) for the S impurity adsorbed on materials of the C2DB database. The ML models are: Linear Regression (first row), Neural Network (second row), Decision Tree (third row), and XGBoost (fourth row). Each model training stage is shown on the left and the testing stage on the right. The dashed red line represents the ideal $y = x$ identity line. Performance metrics, namely, Mean Absolute Error, Mean Squared Error, and the coefficient of determination R^2 , are also shown.

bility, which translates into low energy barriers. Hence, for the ML analyzes here we further restrict the materials to those with energy barriers up to 2.0 eV. This amounts to around 2560 2D systems from the original 4036, i.e., 63% of the total of materials in the C2DB database.

Although semi-empirical calculations tend to display certain differences from the barriers actual values, the global statistical patterns observed in the distributions like, spread, shape, mode position, and average energetic relative order ($\text{Se} > \text{S} > \text{Te}$), comply with known physicochemical traits and with much more sophisticated theoretical and experimental analyses in the literature. This supports the use of our obtained results as reliable input data⁵⁰ to implement ML models. We also recall that the predictors considered for the ML models below (and for the SHAP study in Sec.) are all those mentioned in Sec. , the FSD.

For the ML outcomes presented below, we stress that the parameters of each algorithm were thoroughly tested and tuned to optimize their predictive performance. More concretely, for simpler models, like linear regression and decision trees, various combinations of standard settings were explored, including maximum tree depth, splitting criteria, and normalization strategies. Further, an MLP architecture with various hidden layers was considered for the neural network, and several configurations entailing batch size, activation functions, and optimization schemes were tested. In the case of XGBoost, which delivered the best results, a fine-tuning procedure was carried out using the Optuna library.⁵¹ It allowed an efficient hyperparameter search, targeting the number of estimators, learning rate, maximum depth, and subsampling ratio. Such protocol significantly improved the model accuracy — especially in the testing phase, where generalization capability is critical.

The comparison between the ML models performances yields essentially the same conclusions for the three adsorbing atoms addressed in this work. So, the following discussion focuses on the S case in detail, with only a brief summary provided for Se and Te. The scatter plots in Fig. 5 for S compare the ML predic-

tions (for all the four models investigated) with the calculations of Sec. . In Fig. 5 each row corresponds to one model, with the left (right) panels depicting the training (test) results. The performances are quantified through the Mean Absolute Error (MAE), Mean Squared Error (MSE), and the coefficient of determination (R^2), shown in the corresponding graphs.

For the linear regression in the top row (certainly the simplest ML model), as expected the performance is rather modest, with R^2 equals to 0.336 and 0.163 for the training and testing sets, respectively. It also leads to MAE close to 0.31 eV (training) and a very broad dispersion — refer to the diagonal dashed red line. This stems from a linear fitting trying to describe the nonlinear relationship between the assumed descriptors and the target energy barrier.

The second row in Fig. 5 shows the results for the neural network model based on an MLP architecture. Now, R^2 and MAE are, respectively, 0.368 and 0.286 eV (training) and 0.273 and 0.312 eV (testing). Thus, some improvement is achieved, although still limited. This may be attributed to the relatively simple nature of the input features, based mainly on compositional averages, and dataset size: neural networks are notoriously dependent on significantly large samples, despite being of low computational cost, particularly when coupled with architectural and hyperparameter optimization.⁴³

The decision tree model is presented in the third row of Fig. 5. It has the important feature of partitioning the input space through a hierarchy of decision rules. While leading to $R^2 = 0.430$ during the training stage, it suffered a notable drop in performance during testing, with R^2 decreasing to 0.233 and the MAE increasing from 0.274 eV to 0.327 eV. This behavior suggests overfitting, a well-documented limitation of single decision trees when applied to noisy or highly variable data.⁵² Also, the layer-like pattern in the plots reflects the discrete nature of the model predictions (owned to the countable rules), resulting in a poor representation of any target variable inherently continuous, of course the case of energy barriers.

Finally, the fourth row of Fig. 5 depicts the XGBoost outcomes, outperforming the other

three models in every respect. During training $R^2 = 0.998$, with negligible MAE and MSE, indicating an almost perfect fit. In the testing stage, XGBoost maintains the robustness, with $R^2 = 0.528$, MAE = 0.251 eV, and MSE = 0.108. This success can be attributed to the model ensemble nature, combining many weak learners (shallow decision trees) through gradient boosting to minimize prediction error. XGBoost also incorporates built-in regularization techniques, mitigating overfitting. Such a superiority has already been reported for predicting other material characteristics, e.g., band gaps, formation energies, elastic constants, and thermal coefficients.⁵³

Akin analyzes for Se and Te showed essentially the same qualitative results concerning the efficiency of the distinct ML models, again with XGBoost performing considerably better. For instance, for Se the R^2 values in the test stage were 0.151, 0.309, 0.260, and 0.520 for linear regression, neural network, decision tree, and XGBoost, respectively. For Te, the corresponding values were 0.319, 0.353, 0.313, and 0.540. The full set of calculations for Se and Te are given in the Supplemental Information (SI).

The above upshots demonstrate that while simpler ML schemes, as linear regression and decision trees, offer baseline insights, they lack the required generality and plasticity to unveil the intricate relationships between atomic descriptors and more tangled quantities, the case of energy barriers. Even the more elaborated neural network approach yielded limited gains. On the contrary, XGBoost effectively displayed the proper balance between accuracy and stability to deal with a large and diverse sample of materials.

Examining the ML predictability

Considering the best-performing model, XGBoost, for the relatively broad barrier energy range of 0-2.0 eV, all chalcogen atoms exhibited strong consistency between cross-validation and held-out test performance. This indicates that the adopted hyperparameter optimization and data partitioning strategy effectively migrated information leakage. However, the train-test

error gap remained substantial (~ 0.25 – 0.32 in RMSE), a clear sign of overfitting when the task covers a wide energy range with higher intrinsic variance.

Repeating the XGBoost modeling, but restricting the set of materials to those with barrier energies ≤ 1.5 eV and then to those with ≤ 1.0 eV (in this last case the number of systems being around 1490), the predictive accuracy improved markedly: test RMSE dropped from ~ 0.34 to ~ 0.19 – 0.21 , with MAE following the same trend, indicating that the models capture the structure–property relationship much more reliably for narrower ranges for the barrier energy. Importantly, the train–test gap contracted steadily, from 0.25–0.32 to nearly 0.13–0.17. Further, at a very restrictive regime (< 0.5 eV), roughly representing 500 2D materials, errors reached exceptionally low values (test RMSE 0.09–0.11, MAE 0.07), while the overfitting gap decreased to 0.07–0.10.

Regarding the ML results for the different atoms and for the aforementioned smaller energy windows, Se continuously reduced absolute error and showed the largest decrease in RMSE and MAE. In contrast, Te emerged as the most robust and generalizable element, achieving the highest explained variance (R^2) and the smallest overfitting gap as the target range narrowed. This suggests that for Te, the model captures a broader portion of the underlying variance without holding up spurious details. Finally, S remained a stable baseline with competitive performance and slightly smaller gaps in some intermediate regimes, but it was generally surpassed by Se in raw error and by Te in variance explanation.

As a last technical summary, across all energy thresholds for all atoms, the hyperparameter search consistently selected shallow to moderately deep trees (depth ~ 5 – 6), small learning rates (~ 0.02), and moderate sub-sampling, while increasing regularization and reducing the effective number of boosting rounds as the barrier window narrowed — a coherent adjustment that limits complexity when overfitting risk decreases.

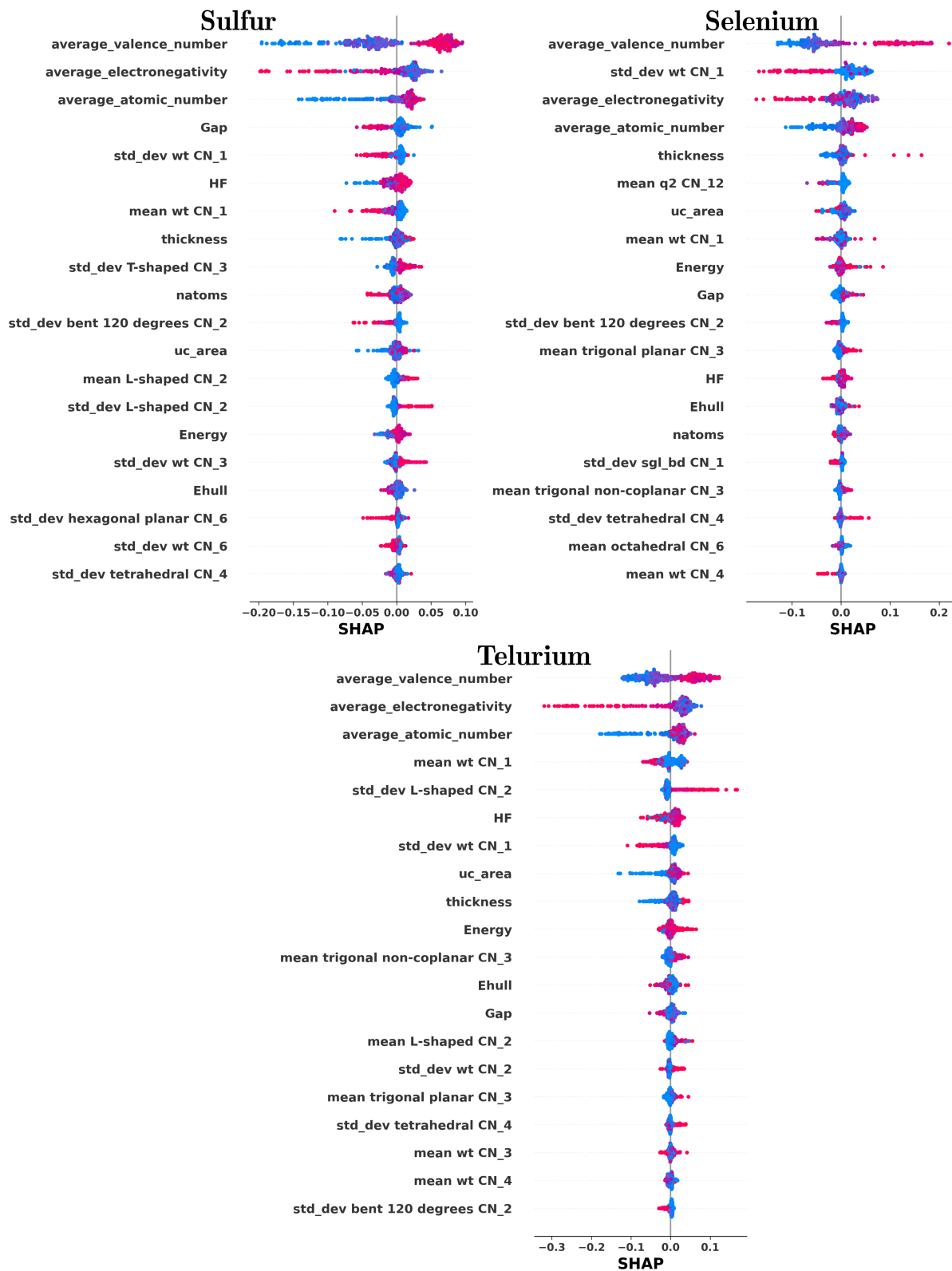


Figure 6: Interpretability analysis using the SHAP protocol applied to the energy barrier estimations from the XGBoost model. The graphs depict the results of adsorption of either S (top left), Se (top right), or Te (bottom) on the two-dimensional systems from the C2DB database with barrier energy ≤ 1.0 eV. Each point represents a distinct 2D material. Predictor features are ranked vertically in descending order of their importance in the model. A predictor variable value is high (low) if its color is pink (blue). The horizontal axis corresponds to the SHAP index. Positive (negative) values tend to increase (decrease) the energy barrier.

Interpretative analyzes

Beyond the standard fitting predictions enabled by ML models, one should not underestimate the importance of their potential interpretability, so that the emerging patterns could, e.g., qualitatively unveil chemical traits. Ideally, a model should provide more than a numerical relationship extrapolating variations in the target variable as a function of the descriptors. It should also possess explanatory power, allowing to attribute concrete physical and hierarchical significance to the observed correlations.

Hence, we shall apply to our results an interpretability protocol based on the usual implementation of the SHAP method. Briefly, rooted in Shapley cooperative game theory, SHAP transforms complex outputs into additive feature contributions, allowing for both local and global interpretations of nonlinear and otherwise opaque ML models (details of its usage and execution can be found in ref.²⁸).

Next, we only consider XGBoost, as it exhibited the best overall performance. Moreover, we restrict the analysis to the better-performing energy regime (≤ 1.0 eV), comprising a set of 1,495 2D structures. For each chalcogen (S, Se, and Te), the results are presented in Fig. 6. The graphs depict the relative contributions of the twenty more relevant predictors — used in the XGBoost model to estimate the energy barriers — ranked in decreasing order of importance, from top to bottom. Each point specifies a given material. The horizontal axes gives the SHAP index value, gauging the feature influence trend on the prediction. A positive (negative) index value indicates that the feature tends to increase (decrease) the barrier energy. A predictor has a higher (lower) value if its color is pinker (bluer).

The relative importance of the top eight descriptors for each chalcogen atom are displayed in the left panels of Fig. 7 — in units of mean modulus SHAP value, horizontal axis. For the other not shown one hundred twenty four descriptors, their combined importance in such unity is 0.32 (S), 0.37 (Se) and 0.36 (Te). Below we mostly discuss and interpret the top seven. Hence, the difference between the seventh and

eighth SHAP index modulus gives an idea of the (somehow arbitrary) cut-off employed.

The SHAP results show that for the S atom, the top seven main influential features are:

- `average_valence_number`
- `average_electronegativity`
- `average_atomic_number`
- `Gap` (band gap)
- `std_dev wt CN_1` (weighted standard deviation for coordination number 1 atoms)
- `HF` (heat of formation)
- `mean wt CN_1` (weighted standard mean of coordination number 1 atoms)

The plots in Fig. 6 reveal that systems with lower average valence number and atomic number and higher electronegativity (observe the colors code) are more likely to exhibit lower barriers — negative SHAP values. This clearly aligns with S higher chemical affinity for more electronegative and compact surfaces. Descriptors associated to surfaces with coordination number one also play a notable role, suggesting (typically) an easier diffusion of S in such structures. Although not among the top seven (see the above list and Fig. 6), local topological features, like `std_dev T-shaped CN_3` (9th) and `std_dev bent 120 degrees CN_2` (11th) are fairly relevant contributors, underscoring the influence of surface geometry in modulating the energy barrier.

For Se, the seven most relevant descriptors are:

- `average_valence_number`
- `std_dev wt CN_1`
- `average_electronegativity`
- `average_atomic_number`
- `thickness`
- `mean q2 CN_12` (mean of the order 2 Steinhardt bond orientation parameter for coordination number 12 atoms)

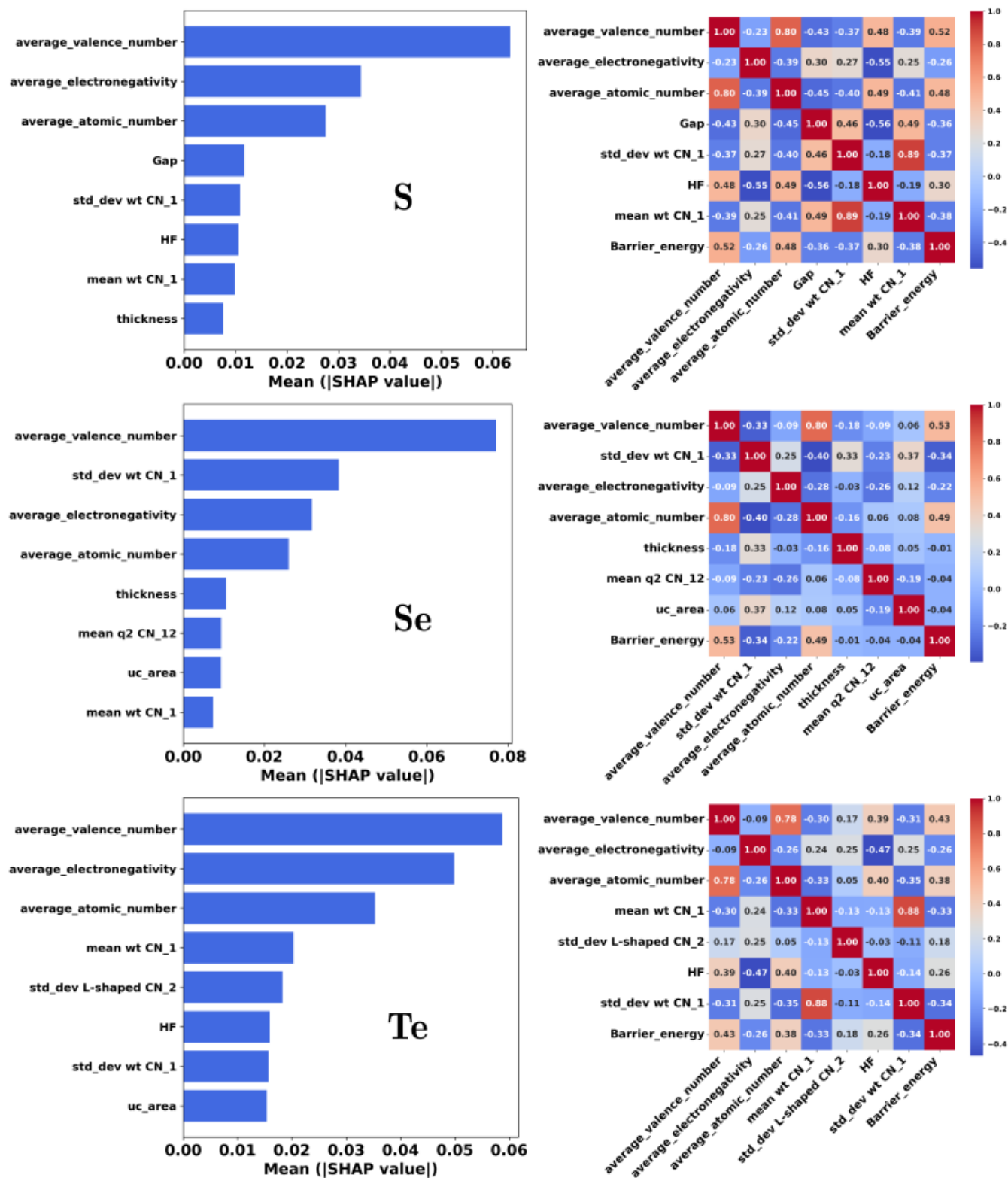


Figure 7: The top eight features from the SHAP analysis (left panels) and the classical Pearson correlation coefficients from the original FSD (right panels), for the 2D materials with S, Se and Te atom impurity. The bar plots rank the most influential descriptors according to their mean absolute SHAP value. The heatmap matrices show the Pearson correlation coefficients between the seven most important features (as identified by SHAP for each atom) and the target barrier energy, computed directly from the FSD without any ML-processing.

- `uc_area` (unit cell area)

Among the eight most important descriptors for Se, six overlap with those for S, although not in the same ranking order. However, Se displays a much higher sensitivity to the local orientation order variable `mean q2 CN_12` and the average valence number feature; compare such a feature SHAP values in Fig. 7, which is around 30% higher for Se. This points to a more substantial role of surface disorder and irregularities, which is consistent with the Se lower electronegativity, resulting in less localized interactions and thus a greater dependence on extended regions of the surface environment. Additionally, thickness and unit cell area are also important descriptors. As seen in Fig. 6, as `thickness` decreases and `uc_area` increases (although with a certain variability) the energy barrier decreases. This reinforces the relationship between morphology and impurity mobility for Se.

For Te, the seven dominant features are:

- `average_valence_number`
- `average_electronegativity`
- `average_atomic_number`
- `mean wt CN_1`
- `std_dev L-shaped CN_2` (standard deviation for L-shaped coordination number 2 atoms)
- `HF`
- `std_dev wt CN_1`

Similar to Se and S, six of the eight most important descriptors for Te and S are identical. Moreover, four of these descriptors also coincide in their relative ranking of importance. This supports the fact that the distributions for S and Te in Fig. 4 are fairly similar. The Te behavior is predominantly governed by average electronic properties, namely, valence, electronegativity, atomic number and even `HF` (6th descriptor), with a less pronounced influence from coordination-specific features, refer to Fig. 7. These traits concur with the Te’s chemical

characteristics as a heavier, more polarizable, and less electronegative element.

More generally, Fig. 6 reveals consistent trends for all the three impurities, while highlighting distinctive tendencies. On one hand, the key electronic descriptors, i.e., average valence, atomic numbers and electronegativity are always among the top four features of S, Se and Te. Therefore, they form the model core foundation, given their strong discriminative power. On the other hand, S and Se show a balanced sensitivity to surface geometry and topology (as coordination type, layer thickness, and local disorder), whereas Te is primarily driven by average electronic properties, with a weaker influence from local structural variations, suggesting a more global and less directional interaction with the 2D surfaces. Also, the moderate relevance of features such as heat of formation (but less important for Se) indicates that thermodynamic stability and temperature-dependent properties should play a certain role in governing impurity diffusion in 2D structures, which is particularly relevant for applications in catalysis, sensing, and 2D-material-based devices.

Pearson correlation of the main descriptors

As an additional, independent, assessment of the SHAP-derived hierarchy of descriptors — further evaluating their predictive power for barrier energy — we computed the corresponding Pearson correlation (see, e.g.,⁵⁴) using the “raw” FSD, i.e., before any ML training.

The correlation matrices for the energy barrier and selected descriptors, the collection of seven features listed above for each chalcogen atom, are depicted in the right panels of Fig. 7 (the energy barrier corresponds to the last row, or equivalently, last column). The color scale indicates both the sign and strength of the relationship. Obviously, a given pair of descriptors does not need to have the same correlation value across the distinct chalcogen atom cases due to the way the correlations are computed⁵⁴ and the collection of variables used.

Comparison between the two types of characterization (SHAP and Pearson) reveals that

the simple calculation of linear statistical correlations, aiming to infer the most relevant quantities for a target property, is a circumscribed procedure. Indeed, the magnitude of a feature impact on the barrier energy as gauged by the “bare” correlation value is not always the same as indicated by SHAP, a much more sophisticated and complete nonlinear interpretability scheme. Notice that since the Pearson matrices have been constructed following the same ordering of predictors by SHAP (left panels), this fact is easy to check by inspecting the bottom row of each matrix. Differently from the SHAP analysis, along it the associated coefficients $|c_{ij}|$ (taken in modulus to comply with the SHAP coefficient, also taken in modulus) do not monotonically decrease (from left to right).

Considering S, i being the `Barrier_energy` and j being (in decreasing order of importance, according to SHAP) `average_valence_number`, `average_electronegativity`, `average_atomic_number`, `Gap`, `std_dev wt CN_1`, `HF`, `mean wt CN_1`, we have, respectively, $|c_{ij}|$ equals to 0.52, 0.26, 0.48, 0.36, 0.37, 0.30, 0.38. Note that `average_electronegativity` (`mean wt CN_1`), the second (7th) most important descriptor, has the lowest (third highest) Pearson correlation, 0.26 (0.38). So, based just on the raw data, one would conclude that `mean wt CN_1` is more important than `average_electronegativity` to establish the barrier energy. Nonetheless, in full agreement with SHAP, investigations in the literature point to the opposite.^{55–57} Furthermore, ordering discrepancy is likewise observed for Se and Te. In particular, even if we restrict to the three top features according to SHAP, they are also classified as the three top by the Pearson correlation only for Se.

The matrices in the right panels of Fig. 7 also show that the correlations between the seven most important predictors have a broad dispersion. While some are well-correlated, others are not. For the case of S, the top five features exhibit a significant degree of mutual correlation, with the smallest $|c_{i \neq j}|$ equal to 0.23. Nonetheless, again considering the top five (even the top four), the variability is much stronger for Se and Te, with the lowest $|c_{i \neq j}|$ ’s being 0.03 and

0.09 for the former and 0.05 and 0.09 for the latter. These findings may suggest that, when considering the strength of their reciprocal correlations, there is no clear pattern for selecting the more pertinent predictors.

However, the above observations do not totally preclude the use of pure statistical measures, such as Pearson’s, to help identify characteristics of appropriate predictors for a model. As an illustration, from the last row of the matrices in Fig. 7 we can calculate the standard deviation σ of $|c_{\text{Barrier_energy } j}|$, with j representing the seven most relevant features for S, Se and Te. We find $\sigma_{\text{Se}} = 0.220 > \sigma_{\text{S}} = 0.092 > \sigma_{\text{Te}} = 0.084$. Although not very different for S and Te, these σ ’s moderately point to a trend: the relative importance of the j ’s is more evenly (unevenly) distributed in the case of Te (Se), with S in the middle way. This qualitatively agrees with the SHAP bar plots in Fig. 7 and at least partially explains the distribution of barrier energies in Fig. 4, which is wider for Se, narrower for S, and even narrower for Te. In fact, given the great diversity of 2D materials analyzed, a higher (lower) variability for the influence of the top predictors should lead to a bigger (smaller) dispersion of the resulting energy barrier, as seen in Fig. 4.

Classifying the materials: a cluster approach for S

The key premise in ML models is that suitably chosen descriptors can adequately estimate a target property, here the barrier energy. Accordingly, depending on the composition and structural characteristics of distinct material groups — determining the values of these predictors — the barrier energy is expected to fall within specific ranges. Conversely, the energies values could reveal systematic differences in the features distributions, providing insight into structure–property classification of the systems, useful in applications.

To explore such possibility, we employ the K-means clustering algorithm to divide the materials in the database according to their impurity mobility driving variables. Similarly to the Pearson correlations, for an independent ana-

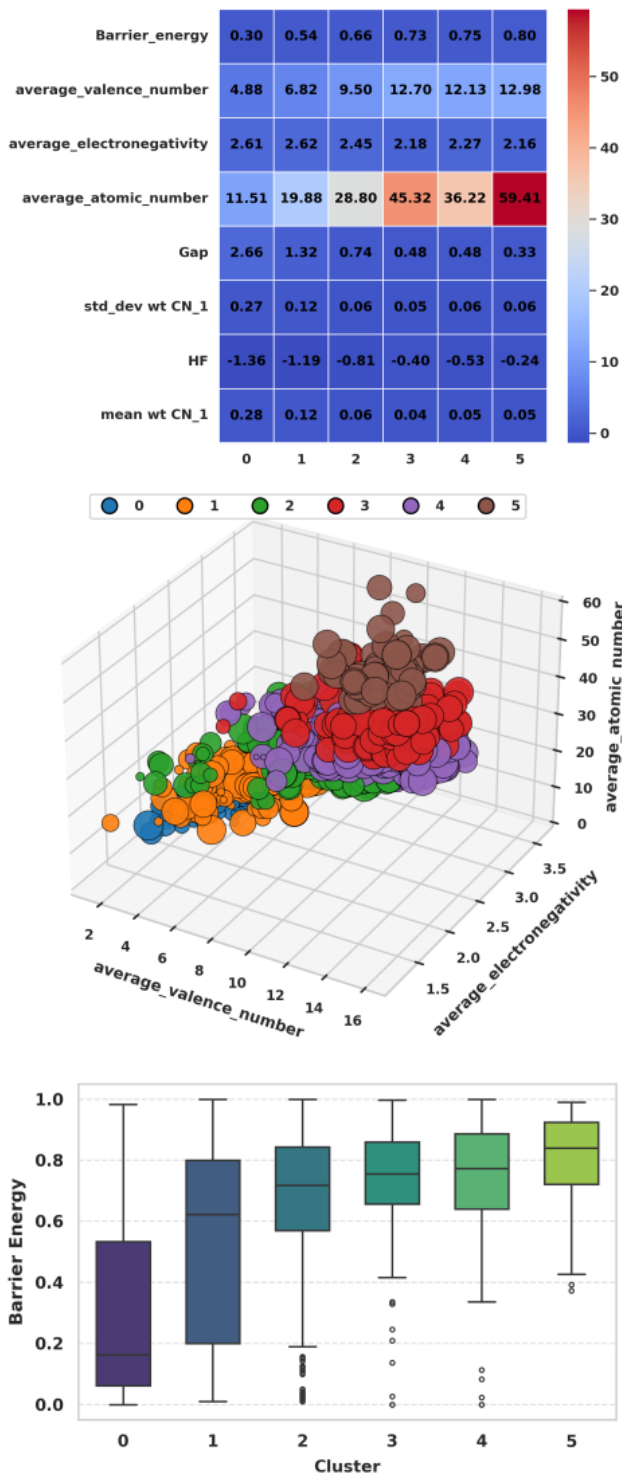


Figure 8: For S, materials of Fig. 7 are classified as cluster 0 to 5 via *K*-means. Top: mean values of barrier energy and of seven relevant predictors (from SHAP) in each cluster. Middle: The materials clustering with the corresponding values of the three top predictors. A bullet size indicates the barrier energy value. Bottom: the barrier energy distribution in each cluster.

lyzes we just address the FSD raw data, i.e., without any ML training. For simplicity, we discuss only S and the 2D systems for which the barrier energy is not superior to 1.0 eV (corresponding to 1,495 materials). We leave Se and Te to the SI.

The *K*-means is an iterative unsupervised protocol that partitions a dataset into collections displaying akin attributes. This is done by calculating either the mean or median of the data specified properties (in our present case, those in FSD). From these quantities, the scheme determines the clusters centroids so that distinct points can be arranged together into different sets. The protocol tries to minimize (maximize) the variance within each cluster (across clusters), so that data points in the same (different) cluster(s) are as similar (dissimilar) as possible. For a complete account on the procedure and implementation details see, e.g., Ref.⁵⁸

The results are summarized in Fig. 8. The method has separated the full collection of 1,495 2D materials into six (the optimal number found) distinct clusters, tagged from 0 to 5. The mean values of the top seven features for S (as classified by SHAP, see top left panel of Fig. 7) as well as of the barrier energy in each cluster are presented as a matrix in Fig. 8. The mean barrier energy increases with the cluster label. In the 3D plot of Fig. 8, each bullet represents a specific material, also indicating the associated values of the top three descriptors. While the bullets colors identify which cluster they belong to, the diameters match the materials barrier energy values. The bar graph of Fig. 8 depicts the distribution of barrier energies in each cluster.

Among the clusters, distinct feature patterns are discernible. For example, the barrier energy average value (the first row of the matrix in Fig. 8) increases through big jumps from clusters 0 to 1 (80.0%) and 1 to 2 (22.2%) and then with smaller variations from 2 to 3 (10.1%), 3 to 4 (2.7%) and 4 to 5 (6.7%) — refer also to the bar chart in Fig. 8. But this consistently relates to the distribution of barrier energy between materials within a cluster. Indeed, 1 and 0 (in this order) exhibit the greatest variations, with 2, 3, 4 and 5 showing reasonably similar narrower

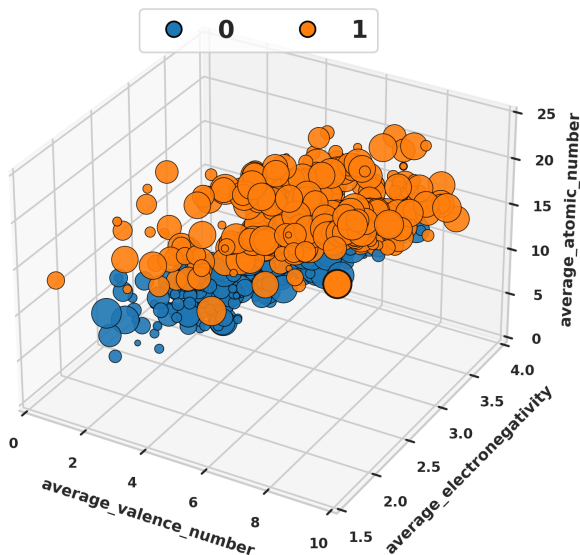


Figure 9: The same as in Fig. 8, but showing only clusters 0 and 1. The plot highlights that materials in these clusters exhibit a broad distribution of electronegativity.

spread.

As for the average values of the seven primary features (matrix in Fig. 8), the first, third and sixth, namely, `average_valence_number`, `average_atomic_number` and HF, increase with the cluster average barrier energy, the exception being for the cluster 4. The fourth descriptor, `Gap`, systematically decreases, again unless for cluster 4. For the first and third descriptors, this also can be verified from the overall trend in the 3D plot of Fig. 8. In particular, notice the broad distribution of the cluster 4 in the `average_valence_number` axis and that typically the materials of cluster 3 are above those for cluster 4 along the `average_atomic_number` axis. We recall that these four predictors are highly correlated, as indicated by the Pearson matrix for S in Fig. 7. The `average_electronegativity` (the second most important descriptor) exhibits a somehow oscillatory trend: it remains nearly constant for clusters 0 and 1, decreases successively for clusters 2 and 3, and then shows a slightly increase followed by a decrease for clusters 4 and 5, with a maximum difference of just 21% across all clusters. The fact that the clusters 0 and 1

present the highest values of electronegativity is difficult to observe from the 3D plot in Fig. 8, but becomes clear from Fig. 9. The remaining two main predictors (fifth and seventh), associated with `NC_1`, exhibit a decaying trait toward a steady value as the mean barrier energy of the clusters increases.

Lastly, we draw a comparison between the *K*-means and the SHAP, emphasizing that they are independent analyses that are not reliant on one another (except from selecting which descriptors to utilize in the former). For so, we recall that in Fig. 6, the pink (blue) color indicates higher (lower) values for the predictors, and that positive (negative) values of the SHAP index points to an increasing (decreasing) of the energy barrier. Thus, from Fig. 6 for S, we clearly see that in agreement with the *K*-means, the energy should increase with the first, second and sixth predictors and decrease with the fourth one. The features associated to `NC_1` tend to decrease the barrier only when they have high values; if they are small, their influence is less relevant (note in Fig. 6 that the blue-coded materials have positive but close to zero SHAP index value). This is in accordance with the clusters characterization for these two descriptors. Finally, as predicted from the *K*-means, the somewhat more complex relationship between `average_electronegativity` and the barrier energy arises from the fact that materials with high values for such predictor can either raise or lower the barrier (see the pink code-color on both sides of the SHAP axis in Fig. 6 for this feature), while the majority of materials with lower values (blue code-color) tend to raise the barrier, albeit mildly. Hence, SHAP and *K*-means are once more in line.

As a final remark, we observe that clustering approaches as the simple and widespread *K*-means (but for more sophisticated ones see, e.g., Ref.⁵⁹) seem to point to the same direction than interpretative protocols, like SHAP. Nonetheless, the advantage of combining ML with interpretative models is to be able to directly determine the descriptors relevance order (refer to Figs. 6 and 7); something not possible by just separating the materials into cluster

classes.

Final Remarks and Conclusion

Over the past two decades, material informatics has emerged as a field that combines AI and data science to explore distinct classes of systems. It focuses on processing information from large datasets to discover and characterize novel materials. With the advent of extensive chemical databases (e.g., C2DB), the combination of ML models, robust statistical methods, new optimization procedures and evolutionary algorithms are enabling more efficient inverse design and automating material analyzes protocols.^{60–62} Along these lines, we could mention the use of various IA strategies for structure forecasting and nanoscale distance estimation with the goal of accelerating costly *ab initio* methods through integration. For instance, crystal structure prediction methods such as USPEX,⁶³ CALYPSO⁶⁴ and AIRSS⁶⁵ have been widely employed. Also, ML platforms have been considered for both classification and regression of interatomic distances (somehow similar to the philosophy in Sec.), like of C–O in lactone derivatives.⁶⁶

In the present contribution we have fully developed a novel framework to study a key aspect of atoms diffusion in 2D systems, the barriers energies. For so, we have struck into a different direction than most investigations. Instead of trying to speed up costly calculations, we sought to enhance semi-empirical quantum methods — here HM — via phenomenologically determining effective equilibrium distances (refer to Eq. (2)); moreover combining the obtained results with supervised ML to improve and speed up the estimation of adsorption energy barriers. In addition, we have used an interpretative protocol to gain concrete physical and chemical insight and ascribe qualitative meaning to the typical black-box-like findings of ML approaches.

We should point out that, in contrast to other considerably more analyzed element classes, such as the already mentioned alkali metal

atoms,^{21–23} here we have chosen to focus on the chalcogen S, Se, and Te impurities on 2D structures, for which there are currently insufficiently detailed studies. Thus, as far as we are aware, this is the most thorough investigation presented in the literature.

Employing the EHM (with a kind of mean global equilibrium distance d_{eq}), we have computed the energy profiles of S, Se, and Te adsorbed on 4,036 systems from the C2DB database. From these profiles, average barriers were defined and considered as target variables for predictive ML models. A diverse set of physicochemical descriptors was extracted using the Matminer library and complemented with extra averaged features related to atomic properties. We have tested distinct ML schemes, but determined that XGBoost consistently outperformed the others in accuracy and generalization capacity. For the ML investigations, the original set of materials have been reduced to those with energy values not superior to 2.0 eV (about 2,560 materials), since lower values tend to attract greater interest in applications.^{9,33,56}

We have verified that further limiting the pull of materials to those with energies not greater than 1.0 eV (1,495 systems) does increase the fitting quality and predictability power. The reason for this is that shifting from a 2.0 eV window to the more concentrated ≤ 1.0 eV region stabilizes the feature hierarchy, decreasing overfitting and increasing generalization while providing a dependable and intelligible link between migration barriers and atomic-scale descriptors.

We have used the SHAP method to characterize the impact of each structural and electronic quantifier on the final energy barriers for the S, Se, and Te impurities for the materials in the latter energy range mentioned above (thus already pertinent for applications; see Introduction section). It has confirmed that for XGBoost, the fitting correlations are chemically meaningful and consistent across impurity types, also capturing the specific migration physics in each case. For instance, as expected, descriptors such as average valence number, electronegativity, and atomic number

were always among the most important in determining the barrier values. However, topological and geometrical features, such as thickness and unit cell area, likewise displayed relevant roles. Regarding morphology, SHAP has shown that overall (see Fig. 6) thinner and denser structures tend to reduce the migration barrier.

Using S as a case study, independent correlation measures have been used to confirm the physical significance of the selected features by SHAP. In particular, Pearson correlation matrices and K-means clustering have effectively validated the consistency of the results reached by the ML plus interpretability scheme. Nevertheless, SHAP has always being superior to any statistical inference method.

Importantly, our framework has successfully uncovered the differences between the chalcogen impurities. For example, the weighted standard deviation at coordination number 1, Fig. 7, shows that Se is more sensitive to local geometric disorder. This suggests that surface imperfections and prolonged structural complexity have a greater influence on Se migration, which is consistent with its lower electronegativity and more diffuse bonding than S.

For Te, the SHAP landscape is broader: the average valence number and average electronegativity dominate, but local topology descriptors (e.g., st. dev. L-shaped CN_2 and weighted st. dev. CN_1) are also relevant, Fig. 7. Since the Te barrier energy is not too strongly dependent on just a small number of features, we should not expect great dispersion of barrier values caused by high variance of only few particular predictors across the distinct materials. This concurs with Fig. 4 (note the plateau-like behavior for Te) and with the heavier, more polarizable character and reduced sensitivity to subtle surface disorder of Te.

To conclude, we bring up two final points. First, the current study demonstrates that, when combined with reliable ML models, semi-empirical approaches provide a workable way to screen adsorption properties in big databases of 2D materials. Moreover, the use of interpretability techniques highlights the role of ML not only as an acceleration tool but also as a way to gain concrete insight into the phe-

nomenology of the process investigated.

Second, it must be noted that the current framework should not be considered the ultimate step in the classification of materials characteristics. Instead, it constitutes a rather fast selection scheme in very large databases. A second stage of analysis would include detailed computations, but then only for the best candidates for determined applications — see, e.g.,⁶⁷ Although along the work we have discussed that generally our outcomes are supported by known results in the literature, ours are naturally not *ab initio* calculations. Thence, some discrepancies in actual numerical values and even in phenomenological behavior might be the case. For instance, eventually for certain particular 2D materials, instead of diffusion, the atom could become “anchored” on the surface, due to the formation of local deep wells, not predicted by the protocols here. Indeed, to determine actual potential profiles we should have a position dependent h_{eq} instead of an effective d_{eq} . We are presently working on a phenomenological h_{eq} based on the idea of topological DCF descriptors,⁶⁸ which hopefully will be reported in the near future.

In summary, the framework’s main benefits are its exceptional speed, versatility, and physical interpretability; being a significant new tool for characterizing the diffusion of atoms in vast databases of 2D materials.

Acknowledgement The authors acknowledge the following financial support. MLPJ: The Foundation of the Federal District (FAP-DF, grant 00193-00001807/2023-16) and the National Council for Scientific and Technological Development (CNPq, grant 444921/2024-9). MGEL: The research grants from CNPq, No. 307512/2023-1 (PQ) and No. 04577/2021-0 (Projeto Universal) as well as the project “Efficiency in uptake, production and distribution of photovoltaic energy distribution as well as other sources of renewable energy sources” (No. 88881.311780/2018-00) via CAPES PRINT-UFPR. PC and MGEL: The 2025 IMI Joint Use Research Program Workshop (I) 2025b007 on the "Advancing Materials Data, Design & Discovery" and

I2CNER. PC is also supported by JSPS KAKENHI Grant-in-Aid for Scientific Research (C) JP24K06797. PC holds an honorary appointment at La Trobe University and is a member of GNAMPA. ALR thanks CAPES/COFECUB grant 88881.188740/2025 – 01 and CNPq under grant numbers 313081/2017 – 4, 305335/2020 – 0, 309599/2021 – 0, and PDPG-FAPDF-CAPES Centro-Oeste grant number 00193 – 00000867/2024 – 94. MJP thanks FAPERGS, grant 24/2551 – 0001551 – 5, CNPq grants 444431/2024 – 1 and 303206/2025 – 0 DGS thanks CNPq grant 409792/2024 – 1 TASP acknowledges support from the National Institute of Science and Technology on Materials Informatics and CNPq - INCT grant 371610/2023 – 0, and FAPEMAT (PRO-2025/00376), CNPq/INCT grant 409174/2024 – 6, and PDPG-FAPDF-CAPES Centro-Oeste grant number 00193 – 00000867/2024 – 94. EAM thanks CNPq, grant number 315324/2023 – 6. CRCR thanks the German Federal Ministry of Education and Research (BMBF) for financial support of the project Innovation-Platform MaterialDigital (www.materialdigital.de) through project funding FKZ number: 13XP5094A. Part of this work was performed on the HoreKa supercomputer funded by the Ministry of Science, Research, and the Arts Baden-Württemberg and by the Federal Ministry of Education and Research. ACD thanks FAPDF, grants 00193 – 00001817/2023 – 43 and 00193 – 00002073/2023 – 84, CNPq grant 305174/2023 – 1, and PDPG-FAPDF-CAPES Centro-Oeste grant number 00193 – 00000867/2024 – 94. RMT acknowledges CNPq for a Research Productivity Fellowship (grant no. 307371/2025-5). All authors acknowledge financial support from CNPq, grant 444069/2024-0.

Supporting Information Available

The Supplementary Information addresses extended results for the Se and Te cases, including performance metrics and prediction plots for all

ML models. Moreover, a detailed interpretability analysis using the SHAP method is also provided. It identifies the most influential descriptors for each impurity. All results are based on the same dataset of 4036 two-dimensional systems from the C2DB database considered here.

References

- (1) Mak, K. F.; Lee, C.; Hone, J.; Shan, J.; Heinz, T. F. Atomically Thin MoS₂: A New Direct-Gap Semiconductor. *Phys. Rev. Lett.* **2010**, *105*, 136805.
- (2) Chhowalla, M.; Shin, H. S.; Eda, G.; Li, L.-J.; Loh, K. P.; Zhang, H. The chemistry of two-dimensional layered transition metal dichalcogenide nanosheets. *Nature Chemistry* **2013**, *5*, 263–275.
- (3) Wang, Q. H.; Kalantar-Zadeh, K.; Kis, A.; Coleman, J. N.; Strano, M. S. Electronics and optoelectronics of two-dimensional transition metal dichalcogenides. *Nature Nanotechnology* **2012**, *7*, 699–712.
- (4) Manzeli, S.; Ovchinnikov, D.; Pasquier, D.; Yazyev, O. V.; Kis, A. 2D transition metal dichalcogenides. *Nature Reviews Materials* **2017**, *2*, 17033.
- (5) Zhao, P.; Jian, M.; Zhang, Q.; Xu, R.; Liu, R.; Zhang, X.; Liu, H. A new paradigm of ultrathin 2D nanomaterial adsorbents in aqueous media: graphene and GO, MoS₂, MXenes, and 2D MOFs. *Journal of Materials Chemistry A* **2019**, *7*, 16598–16621.
- (6) Dou, M.; Fyta, M. Lithium adsorption on 2D transition metal dichalcogenides: towards a descriptor for machine learned materials design. *Journal of Materials Chemistry A* **2020**, *8*, 23511–23518.
- (7) Avasarala, S.; Bose, S. 2D nanochannels and huge specific surface area offer unique ways for water remediation and adsorption: assessing the strengths of hexagonal boron nitride in separation technology.

- Functional Composite Materials* **2023**, *4*, 5.
- (8) Sahithi, A.; Sumithra, K. Adsorption and sensing of CO and NH₃ on chemically modified graphene surfaces. *RSC Advances* **2020**, *10*, 42318–42326.
- (9) Han, S. A.; Bhatia, R.; Sang-Woo, K. Synthesis, properties and potential applications of two-dimensional transition metal dichalcogenides. *Nano Convergence* **2015**, *2*, 17.
- (10) Zhao, Y.; González-García, N.; Truhlar, D. G. Benchmark Database of Barrier Heights for Heavy Atom Transfer, Nucleophilic Substitution, Association, and Unimolecular Reactions and Its Use to Test Theoretical Methods. *The Journal of Physical Chemistry A* **2005**, *109*, 2012–2018.
- (11) Spiekermann, K.; Pattanaik, L.; Green, W. H. High accuracy barrier heights, enthalpies, and rate coefficients for chemical reactions. *Scientific Data* **2022**, *9*, 417.
- (12) Gjerding, M. N. et al. Recent progress of the Computational 2D Materials Database (C2DB). *2D Materials* **2021**, *8*, 044002.
- (13) Hoffmann, R. An Extended Hückel Theory. I. Hydrocarbons. *The Journal of Chemical Physics* **1963**, *39*, 1397–1412.
- (14) Ammeter, J. H.; Bürgi, H. B.; Thibault, J. C.; Hoffmann, R. Counterintuitive orbital mixing in semiempirical and ab initio molecular orbital calculations. *Journal of the American Chemical Society* **1978**, *100*, 3686–3692.
- (15) Farrar, E. H. E.; Grayson, M. N. Machine learning and semi-empirical calculations: a synergistic approach to rapid, accurate, and mechanism-based reaction barrier prediction. *Chemical Science* **2022**, *13*, 7594–7603.
- (16) Liang, Z.; Fan, X.; Singh, D. J.; Zheng, W. T. Adsorption and diffusion of Li with S on pristine and defected graphene. *Physical Chemistry Chemical Physics* **2016**, *18*, 31268–31276.
- (17) Dysart, A. D.; Burgos, J. C.; Mistry, A.; Chen, C.-F.; Liu, Z.; Hong, C. N.; Balbuena, P. B.; Mukherjee, P. P.; Pol, V. G. Towards Next Generation Lithium-Sulfur Batteries: Non-Conventional Carbon Compartments/Sulfur Electrodes and Multi-Scale Analysis. *Journal of The Electrochemical Society* **2016**, *163*, A730.
- (18) Ren, Y.; Zhai, Q.; Wang, B.; Hu, L.; Ma, Y.; Dai, Y.; Tang, S.; Meng, X. Synergistic Adsorption-Electrocatalysis of 2D/2D heterostructure toward high performance Li-S batteries. *Chemical Engineering Journal* **2022**, *439*, 135535.
- (19) Tong, Y.; Oughaddou, H.; Enriquez, H.; Kubsky, S.; Esaulov, V.; Bendounan, A. Adsorption of Se on Cu(100) and formation of two-dimensional copper selenide layer. *Materials Today: Proceedings* **2021**, *39*, 1170–1174.
- (20) Sharma, T.; Sharma, S.; Sharma, M.; Sharma, R. Adsorption of Te clusters on tellurene and MoS_2 monolayers: structural, electronic, and optical properties. *Journal of Nanoparticle Research* **2024**, *26*, 75.
- (21) Olsson, E.; Chai, G.; Dove, M.; Cai, Q. Adsorption and migration of alkali metals (Li, Na, and K) on pristine and defective graphene surfaces. *Nanoscale* **2019**, *11*, 5274–5284.
- (22) Heidari, S.; Esrafil, M. D.; Sardroodi, J. J. Li, Na and K storage capacity of a novel 2D graphitic carbon-nitride membrane, C₉N₄: A computational approach. *Chemical Physics Letters* **2023**, *817*, 140414.
- (23) Ullah, S.; Denis, P. A.; Sato, F. Adsorption and diffusion of alkali-atoms (Li, Na,

- and K) on BeN dual doped graphene. *International Journal of Quantum Chemistry* **2019**, *119*, e25900.
- (24) Butler, K. T.; Davies, D. W.; Cartwright, H.; Isayev, O.; Walsh, A. Machine learning for molecular and materials science. *Nature* **2018**, *559*, 547–555.
- (25) Ward, L. et al. Matminer: An open source toolkit for materials data mining. *Computational Materials Science* **2018**, *152*, 60–69.
- (26) Chen, T.; Guestrin, C. XGBoost: A Scalable Tree Boosting System. Proceedings of the 22nd ACM SIGKDD International Conference on Knowledge Discovery and Data Mining. New York, NY, USA, 2016; p 785–794.
- (27) Zhang, Y.; Ling, C. A strategy to apply machine learning to small datasets in materials science. *npj Computational Materials* **2018**, *4*, 25.
- (28) Lundberg, S. M.; Lee, S.-I. A Unified Approach to Interpreting Model Predictions. Advances in Neural Information Processing Systems. 2017.
- (29) Rodríguez-Pérez, R.; Bajorath, J. Interpretation of Compound Activity Predictions from Complex Machine Learning Models Using Local Approximations and Shapley Values. *Journal of Medicinal Chemistry* **2020**, *63*, 8761–8777.
- (30) Avery, P.; Ludowieg, H.; Autschbach, J.; Zurek, E. Extended Hückel calculations on solids using the Avogadro molecular editor and visualizer. 2018.
- (31) Liu, J.; Ren, J.-C.; Li, S.; Liu, W. Role of van der Waals interactions on the binding energies of 2D transition-metal dichalcogenides. *Applied Surface Science* **2023**, *608*, 155163.
- (32) Fukaya, Y.; Zhao, Y.; Kim, H.-W.; Ahn, J. R.; Fukidome, H.; Matsuda, I. Atomic arrangements of quasicrystal bilayer graphene: Interlayer distance expansion. *Physical Review B* **2021**, *104*, L180202.
- (33) Gao, B.; Shao, X.; Jian, L.; Wang, Y.; Ma, Y. Structure Prediction of Atoms Adsorbed on Two-Dimensional Layer Materials: Method and Applications. *The Journal of Physical Chemistry C* **2015**, *119*, 20111–20118.
- (34) Bian, R.; Li, C.; Liu, Q.; Cao, G.; Fu, Q.; Meng, P.; Zhou, J.; Liu, F.; Zheng, L. Recent progress in the synthesis of novel two-dimensional van der Waals materials. *National Science Review* **2022**, *9*, nwab164.
- (35) Batsanov, S. S. Van der Waals radii of elements. *Inorganic Materials* **2001**, *37*, 871–885.
- (36) Rokni, H.; Lu, W. Direct measurements of interfacial adhesion in 2D materials and van der Waals heterostructures in ambient air. *Nature Communications* **2020**, *11*, 5607.
- (37) Duffy, J.; Lawlor, J.; Lewenkopf, C.; Ferreira, M. S. Impurity invisibility in graphene: Symmetry guidelines for the design of efficient sensors. *Physical Review B* **2016**, *94*, 045417.
- (38) Cariglia, M.; Giambò, R.; Perali, A. Electronic properties of curved few-layers graphene: a geometrical approach. *Condensed Matter* **2018**, *3*, 11.
- (39) Batsanov, S. S. Relationship between the Covalent and Van der Waals Radii of Elements. *Russian Journal of Inorganic Chemistry* **2001**, *46*, 1374–1375.
- (40) Alvarez, S. A cartography of the van der Waals territories. *Dalton Transactions* **2013**, *42*, 8617.
- (41) Li, Q.; Fu, N.; Omeo, S. S.; Hu, J. MD-HIT: Machine learning for material property prediction with dataset redundancy control. *npj Computational Materials* **2024**, *10*, 245.

- (42) Kuhn, M.; Johnson, K.; others *Applied predictive modeling*; Springer, 2013; Vol. 26.
- (43) Schmidhuber, J. Deep learning in neural networks: An overview. *Neural Networks* **2015**, *61*, 85–117.
- (44) Kingsford, C.; Salzberg, S. L. What are decision trees? *Nature Biotechnology* **2008**, *26*, 1011–1013.
- (45) Choudhary, K.; DeCost, B.; Chen, C.; Jain, A.; Tavazza, F.; Cohn, R.; Park, C. W.; Choudhary, A.; Agrawal, A.; Billinge, S. J. L.; Holm, E.; Ong, S. P.; Wolverton, C. Recent advances and applications of deep learning methods in materials science. *npj Computational Materials* **2022**, *8*, 59.
- (46) Stark, M. S.; Kuntz, K. L.; Martens, S. J.; Warren, S. C. Intercalation of Layered Materials from Bulk to 2D. *Advanced Materials* **2019**, *31*, 1808213.
- (47) Hou, T.; Zeng, W.; Zhou, Q. Adsorption Mechanism of SO₂ on Transition Metal (Pd, Pt, Au, Fe, Co and Mo)-Modified InP₃ Monolayer. 2022; <https://doi.org/10.3390/chemosensors10070279>.
- (48) Bernard Rodríguez, C. R.; Santana, J. A. Adsorption and diffusion of sulfur on the (111), (100), (110), and (211) surfaces of FCC metals: Density functional theory calculations. *The Journal of Chemical Physics* **2018**, *149*, 204701.
- (49) Nascimento, K. S.; Alves, H. W. L.; Scolfaro, L. Theoretical study of Sn and Te adsorption over graphene from ab initio calculations. *AIP Advances* **2020**, *10*, 105313.
- (50) Mohammed, S.; Budach, L.; Feuerpfeil, M.; Idhe, N.; Nathansen, A.; Noack, N.; Patzlaff, H.; Naumann, F.; Harmouch, H. The effects of data quality on machine learning performance on tabular data. *Information Systems* **2025**, *132*, 102549.
- (51) Akiba, T.; Sano, S.; Yanase, T.; Ohta, T.; Koyama, M. Optuna: A Next-generation Hyperparameter Optimization Framework. Proceedings of the 25th ACM SIGKDD International Conference on Knowledge Discovery & Data Mining. New York, NY, USA, 2019; p 2623–2631.
- (52) Quinlan, J. R. Induction of decision trees. *Machine Learning* **1986**, *1*, 81–106.
- (53) Xie, T.; Grossman, J. C. Crystal Graph Convolutional Neural Networks for an Accurate and Interpretable Prediction of Material Properties. *Physical Review Letters* **2018**, *120*, 145301.
- (54) Felipe, H.; Viol, A.; Araujo, D. B.; da Luz, M. G. E.; Palhano-Fontes, F.; Onias, H.; Raposo, E. P.; Viswanathan, G. M. Threshold-free estimation of entropy from a Pearson matrix. *EPL* **2023**, *141*, 31003.
- (55) Gao, W.; Chen, Y.; Li, B.; Liu, S.-P.; Liu, X.; Jiang, Q. Determining the adsorption energies of small molecules with the intrinsic properties of adsorbates and substrates. *Nature Communications* **2020**, *11*, 1196.
- (56) Lee, B. H.; Fatheema, J.; Akinwande, D.; Wang, W. Understanding and predicting trends in adsorption energetics on monolayer transition metal dichalcogenides. *npj 2D Materials and Applications* **2025**, *9*, 61.
- (57) Shaw, P. K.; Taraporewalla, J.; Raza, S.; Kumar, A.; Duttagupta, R.; Rahaman, H.; Saha, D. Adsorption of Mo and O at S-vacancy on ReS₂ surface of ReS₂/MoTe₂ vdW heterointerface. *Chemical Physics Impact* **2025**, *10*, 100817.
- (58) Ikotun, A. M.; Ezugwu, A. E.; Abualigah, L.; Abuhaija, B.; Heming, J. K-means clustering algorithms: A comprehensive review, variants analysis, and advances in the era of big data. *Information Sciences* **2023**, *622*, 178.

- (59) Wosniack, M. E.; Santos, M. C.; Raposo, E. P.; Viswanathan, G. M.; da Luz, M. G. E.; Schulman, L. S. Identifying dynamical structures in the physical space of stochastic processes. *Europhysics Letters* **2019**, *125*, 20004.
- (60) Liu, Y.; Niu, C.; Wang, Z.; Gan, Y.; Zhu, Y.; Sun, S.; Shen, T. Machine learning in materials genome initiative: A review. *Journal of Material Research and Technology* **2020**, *57*, 113.
- (61) Kulik, H. J.; *et al* Roadmap on Machine learning in electronic structure. *Electronic Structure* **2022**, *4*, 023004.
- (62) Mannodi-Kanakkithodi, A.; Pilania, G.; Huan, T. D.; Lookman, T.; Ramprasad, R. Machine Learning Strategy for Accelerated Design of Polymer Dielectrics. *Scientific Reports* **2016**, *6*, 20952.
- (63) Glass, C. W.; Oganov, A. R.; Hansen, N. USPEX – evolutionary crystal structure prediction. *Computer Physics Communications* **2006**, *175*, 713.
- (64) Wang, Y.; Lv, J.; Zhu, L.; Ma, Y. CALYPSO: A method for crystal structure prediction. *Computer Physics Communications* **2012**, *183*, 2063.
- (65) Pickard, C. J.; Needs, R. J. Ab initio random structure searching. *Journal of Physics: Condensed Matter* **2011**, *23*, 053201.
- (66) Nguyen, L. T. H.; Fukumoto, Y.; Cesana, P.; Staykov, A. Fully Automated Optimization of Ring-Opening Reactions in Lactone Derivatives via Two-Step Machine Learning. *The Journal of Physical Chemistry A* **2023**, *127*, 10159.
- (67) Tian, S.; Zhou, K.; Yin, W.; Liu, Y. Machine learning enables the discovery of 2D Invar and anti-Invar monolayers. *Nature Communications* **2024**, *15*, 6977.
- (68) Tromer, R. M. Dynamic collision fingerprints (DCF): introducing a new descriptor linking lattice interactions to 2D structural data signatures. *Journal of Chemical Theory and Computation* **2025**, *21*, 8106.